The Alexander Disease Protein GFAP Drives Mitochondrial Fission

Ding XIONG[1, 2, †, *], Linghai KONG[3, 4, 5, †], Ye Sing TAN[1], Fang YUAN[1], Zijun SUN[3, 4, 5], Xueyan LI[3,4,5], Emily ABELLA[3,4,5], Albee MESSING[3,6], Su-Chun ZHANG[1, 3, 4, 5, *]

[1]Program in Neuroscience & Behavioural Disorders, Duke-NUS Medical School; 169857 Singapore, Singapore.

[2]State Key Laboratory of Oral Diseases, National Clinical Research Center for Oral Diseases, West China Hospital of Stomatology, Sichuan University; Chengdu, 610041, China.

[3]Waisman Center, University of Wisconsin-Madison; Madison, WI 53705, USA.

[4]Department of Neuroscience, School of Medicine and Public Health, University of Wisconsin-Madison; Madison, WI 53705, USA.

[5]Department of Neurology, School of Medicine and Public Health, University of Wisconsin-Madison; Madison, WI 53705, USA.

[6]Department of Comparative Biosciences, School of Veterinary Medicine, University of Wisconsin-Madison; Madison, WI 53705, USA.

[†]These authors contributed equally to this work.

*Corresponding author. Email: suchun.zhang@wisc.edu or xiongding@u.nus.edu

Abstract

Mitochondrial plasticity, coordinated by fission and fusion, is crucial to ensure cellular functions. Mitochondrial fission is mediated by the GTPase Drp1 at the constriction site, which is proposed to be driven by the actin-myosin contractile force. However, the mechanism that propels constriction remains unclear, and the potential involvement of additional mechanisms in this process remains an open question. Here, using structured illumination microscopy and electron microscopy, we show that the type-III intermediate filament glial fibrillary acidic protein (GFAP) closely surrounds mitochondria fission sites and associates with accumulated Drp1 molecules. Remarkably, loss of GFAP results in hyperfused mitochondria under physiological condition and even Ca^{2+}-induced mitochondrial fission. Additionally, mutations of GFAP, the cause of Alexander disease, result in an elevated recruitment of Drp1 to GFAP, leading to significantly increased mitochondrial fissions. Taking together, these findings suggest a novel mechanism of mitochondrial division mediated by type-III intermediate filaments.

Mitochondria are highly dynamic in responding to cellular states, and this dynamic process is primarily regulated through fission and fusion[1]. Normal mitochondrial fission ensures cellular homeostasis, while excessive fission is often associated with major diseases, particularly neurodegenerative diseases[2,3,4]. Mitochondrial fission is a multi-step process in which the fission sites are marked by endoplasmic reticulum (ER) tubules followed by GTPase Drp1-mediated cleavage[5,6,7,8]. Given that the diameter of Drp1 spirals (30-50 nm) is significantly smaller than that of mitochondria (0.5-1 μm), a pre-constriction is necessary and actin filaments are proposed to facilitate constriction in a subset of fission routes [9,10,11,12]. However, their necessity but not sufficiency with unclear mechanisms raises possible involvement of additional apparatuses.

Intermediate filaments (IFs) form elaborate networks, providing tensile strength and anchoring organelles, and demonstrate cell-type specific expression profiles[13,14,15,16,17]. In brain astrocytes, GFAP is the most abundant IFs. GFAP upregulation is nearly a universal feature under neurological conditions but the regulatory mechanism is unknown [18]. Importantly, GFAP mutations result in astrocyte dysfunction, neuronal degeneration, and demyelination, leading to the often fatal Alexander disease (AxD)[19,20]. RNA sequencing of human astrocytes with AxD mutations revealed alterations in mitochondria function and metabolic pathway[21], suggesting a role of GFAP in mitochondrial function. Although other IFs such as vimentin have been shown to interact with mitochondria[13], whether and how IFs regulate mitochondria function remains unknown. Pathologically, how the disease-causing mutations in IFs affect mitochondria is an open question.

Mitochondria align with GFAP filaments

To address these questions, we differentiated astrocytes from human pluripotent stem cells (hPSCs, H1 embryonic stem cell line) as previously described[22]. Following a 14-day maturation in the presence of bone morphogenetic protein 4 (BMP4) and ciliary neurotrophic factor (CNTF) (**Fig. 1A**), the resulting astrocytes exhibited a star-shaped morphology with radial processes reminiscent of human astrocytes *in vivo* (**fig. S1A**). Using structured illumination microscopy (SIM), we observed GFAP filaments organized into a highly ordered fashion (**Fig. 1B**). These filaments exhibited a parallel alignment, forming thick bundles (0.52±0.13 μm in thickness under light microscopy, **fig. S1B**), and extended from the cell center to the processes **(Fig. 1B, box 1)**, while in the area between the astrocyte processes,

fewer individual GFAP filaments showed a less directional orientation (0.18±0.02 μm) **(Fig. 1B, box 2)**.

We next examined the spatial relationship between endogenous GFAP and mitochondria (labeled by Tomm20) and found that mitochondria were 'embedded' among GFAP filaments: they looked being wrapped by GFAP filaments and aligned in a highly parallel fashion along GFAP filaments, especially at the region with dense GFAP filaments (**Fig. 1C, box 1)**. This alignment was confirmed by the Mander's coefficient quantification **(Fig. 1D)**. In regions with sparse individual GFAP filaments, there were few mitochondria. Nevertheless, they were still localized along GFAP filaments (**Fig. 1C, box 2**). We further confirmed such spatial distribution by visualizing GFAP via expression of WT-GFAP-mNeon under the GFAP promoter and mitochondria with MitoTracker (**Fig. 1E**). Quantitatively, majority of mitochondria aligned with the GFAP bundles, fewer with individual GFAP filaments, and only 2% of mitochondria appeared unassociated with GFAP (**Fig. 1F**). This colocalization was corroborated by transmission electron microscopy, through which we observed that mitochondria were wrapped by GFAP filaments (**Fig. 1G**). Thus, mitochondria closely align with GFAP filaments within human astrocytes.

GFAP knockout inhibits mitochondrial fission

The close spatial vicinity between GFAP and mitochondria suggests that they may interact dynamically. Therefore, we performed live-imaging to assess mitochondrial dynamics in wildtype and GFAP knockout astrocytes. We generated a GFAP knockout cell line using the H1 embryonic stem cell by CRISPR, followed by differentiation into astrocytes **(fig. S2A-B)**. The absence of GFAP in the differentiated astrocytes was confirmed by western blot and immunostaining (**fig. S2C-D**). The astrocyte identity was validated by additional astrocyte markers, such as SOX9 and S100β (**fig. S2E**). Significantly, mitochondria underwent morphological change in GFAP knockout astrocytes. We categorized them based on size and shape characters as follows: fragmented (small or round), intermediate (medium size with round and tubular shape), and tubulated (long and higher interconnectivity)[23,24]. Among the isogenic control cells, the majority (79%) exhibited an intermediate mitochondrial phenotype **(Fig. 2A)**, with an average mitochondrial length of 10.3±2.7 μm **(Fig. 2C)**. Strikingly, in GFAP knockout astrocytes, the majority (83%) displayed tubular mitochondria with a significantly increased length at 37.1±8.1 μm, indicative of mitochondrial hyperfusion (**Fig. 2B-C)**.

99 Correspondingly, the number of mitochondria in GFAP knockout astrocytes was drastically
100 lower compared to that of control astrocytes **(Fig. 2D)**. The phenotype of mitochondrial
101 hyperfusion in GFAP knockout astrocytes is likely due to the failure of fission or enhancement
102 of fusion[6,25,26], and indicates that GFAP critically regulates the balance of these antagonistic
103 reactions. Indeed, expression of GFAP under a GFAP promoter rescued the phenotype in the
104 GFAP knockout astrocytes, with a majority (64%) of astrocytes exhibiting an intermediate
105 mitochondrial characteristic (**Fig. 2E**).
106
107 To discern whether the role of GFAP in mitochondrial dynamics is achieved through promoting
108 fission or inhibiting fusion, we examined mitochondrial dynamics by an assay based on
109 thapsigargin-stimulated mitochondrial fission. Thapsigargin triggers mitochondrial fission
110 through the activation of calcineurin and subsequent dephosphorylation of Drp1 via Ca^{2+}
111 release[27,28]. As a control, 97% of wildtype astrocytes underwent mitochondrial fission within
112 1-3 hours after treatment with thapsigargin **(Fig. 2F, movie. S1)**. If GFAP's role is driving
113 fission, thapsigargin treatment would not stimulate fission in the absence of GFAP; conversely,
114 if GFAP functions by inhibiting fusion, thapsigargin treatment could stimulate mitochondria
115 fission without GFAP. Interestingly, in the GFAP knockout astrocytes, mitochondria
116 maintained the tubulated form and showed no response to thapsigargin stimulation for more
117 than 7 hours (121/130 cells) **(Figure 2F, fig. S3A, movie. S1),** indicating a loss of fission.
118 Therefore, our data support that GFAP promotes mitochondrial fission instead of inhibiting
119 fusion. To determine how loss of GFAP results in unsuccessful fission, we examined two
120 possibilities: 1) the decrease in Ca^{2+} release and 2) loss of Drp1 accumulation. Live-imaging
121 of cytosolic Ca^{2+} ruled out the possibility of Ca^{2+} release inhibition, as both GFAP knockout
122 and control astrocytes showed acute Ca^{2+} increase immediately upon thapsigargin treatment
123 and equilibrated to comparable level within 15min **(fig. S3B)**. However, immunostaining of
124 Drp1 revealed decreased Drp1 puncta on mitochondria in GFAP knockout astrocytes **(fig.
125 S3C),** while no changes were observed in the fusion protein Mfn1/2 on mitochondria **(fig.
126 S3D)**. These results suggest a potential role of GFAP in regulating mitochondrial fission
127 machinery, likely through presenting Drp1 to mitochondria.
128
129 **Mitochondrial fission is enhanced by AxD mutations**
130 In humans, GFAP mutations cause a rare yet often fatal Alexander disease (AxD), a complex
131 leukodystrophy characterized by dysfunctional astrocytes which ultimately lead to
132 neurodegeneration[19]. The above findings led us to hypothesize that mutant forms of GFAP

133 disrupt mitochondrial distribution and fission/fusion dynamics in AxD patient astrocytes. We
134 generated astrocytes from two AxD patients' induced pluripotent stem cells (iPSCs) carrying
135 the C88 and W416 mutations, as well as their respective isogenic control cell lines (R88 and
136 R416) via CRISPR-mediated genetic correction[21]. In contrast to the radial distribution of
137 mitochondria from the cell center to peripheral regions in isogenic control astrocytes,
138 mitochondria in astrocytes with both C88 and W416 mutations exhibited a scattered
139 distribution throughout the cytoplasm **(Fig. 3A)**. However, the mutation did not alter the
140 alignment of mitochondria with GFAP filaments (**fig. S4**). Interestingly, in contrast to GFAP
141 knockout astrocytes, the vast majority of AxD astrocytes (91%) displayed fragmented
142 mitochondria, while the isogenic control astrocytes predominantly exhibited intermediate
143 mitochondria (80% and 91% in R88 and R416 isogenic groups, respectively) **(Fig. 3A)**.
144 Quantification of the length of individual mitochondria revealed notably shorter length in AxD
145 astrocytes (3.9±1.1 μm for C88 mutant, 3.3±2.4 μm for W416 mutant) than in isogenic
146 astrocytes (15.7±7.2 μm for R88 control, 10.3±2.2 μm for R416 control) **(Fig. 3B)**. Thus,
147 GFAP mutations alter the distribution and fission/fusion dynamics of mitochondria.
148
149 Next, we investigate how mitochondrial dynamics is altered by the mutant GFAP. We
150 synchronized the mitochondrial state by thapsigargin treatment followed by its washout. We
151 found no difference between AxD and isogenic control cells in thapsigargin induced
152 mitochondrial fragmentation (90/94 cells in R88 group, 146/152 cells in C88 group; 91 /101 in
153 R416 group, 85/97 in W416 group) **(fig. S5a, movie. S2)**, indicating that the fission machinery
154 is functional in both AxD and isogenic control astrocytes. After thapsigargin withdrawal,
155 mitochondria elongation started in ~3 hours in both AxD and control astrocytes (3.8±1.6 hours
156 in R88 group, 2.9±1.0 hours in C88 group) **(Fig. 3C-D)**, suggesting that the mitochondrial
157 fusion machinery is unlikely affected by the GFAP mutation. Over a 22-hour tracking period,
158 92% control astrocytes formed hyperfused mitochondria (in agreement with previous study in
159 rat liver cells[27]), whereas only 25% AxD astrocytes formed hyperfused mitochondria and the
160 remaining fused to "intermediate" mitochondria **(Fig. 3C, movie. S3)**. Besides, after
161 mitochondrial elongation, the majority of AxD astrocytes rapidly reverted to fragmented
162 mitochondria at ~12 hours, much earlier than the control astrocytes which transitioned back to
163 the intermediate state at ~18 hours **(Fig. 3D)**. These dynamic changes were also reflected by
164 the length of individual mitochondria within single cells analyzed at five time points, indicating
165 that GFAP mutation correlates with an enhanced mitochondrial fission activity **(Fig. 3E-F, fig.**

166 **S5B)**. A similar phenotype was also seen in astrocytes with the W416 mutation **(fig. S5C-E)**,
167 indicating that the increased fission is a consistent phenotype from AxD GFAP mutations.
168 Thus, GFAP mutations primarily upregulate mitochondrial fission.
169
170 **GFAP filaments directly participate in mitochondrial constriction**
171 To uncover the mechanisms underlying the role of GFAP in mitochondrial fission, we assessed
172 their spatiotemporal interaction using structured illumination microscopy. we noticed that
173 mitochondria with a narrowing diameter is at the site where GFAP filament crossed (**Fig. 4A)**.
174 This observation was corroborated by electron microscopy, revealing the intertwining of the
175 ER tubules and GFAP filaments around the constricted "neck" of dividing mitochondria (**Fig.**
176 **4B**), which suggests that GFAP filaments may participate in mitochondrial constriction. By
177 live-cell imaging of astrocytes expressing the fluorescent-tagged GFAP (WT-GFAP-mNeon
178 or mutant C88-GFAP-mNeon) (**fig. S6A)**, we observed that GFAP filaments crossed and
179 scanned/slid along mitochondria during the constriction process (**Fig. 4C-G, fig. S6B-D,**
180 **movie. S4-5**). Notably, the constriction of mitochondria was spatiotemporally coupled with the
181 movement of GFAP filaments along mitochondria (**Fig. 4D-E, fig. S6B, movie. S4**). Further
182 quantification showed that majority of fission events (83% in WT-GFAP expressing astrocytes
183 and 86% in C88-GFAP expressing astrocytes) occurred at locations where GFAP filaments
184 intersected with mitochondria. This was confirmed by measuring the fluorescence intensity of
185 GFAP and mitochondria perpendicular to the fission sites (**Fig. 4D, G**). The tight association
186 of GFAP filament with mitochondria covering the constriction process indicates that
187 intermediate filament-mitochondria contact is important particularly at the early, constriction
188 stage. In contrast, when mitochondria were aligned in parallel with GFAP, we observed few
189 fission events (**fig. S6E**). These results indicate that GFAP filaments participate in
190 mitochondrial constriction during the fission process.
191
192 **GFAP filaments serve as scaffolds for fission protein Drp1**
193 Mitochondrial constriction is followed by Drp1 GTPase-mediated cleavage to achieve fission[5].
194 The fact that both wildtype and mutant GFAP filaments exert constriction similarly (**Fig. 4**)
195 but AxD patient astrocytes exhibit more pronounced mitochondrial fission (**Fig. 3**) raised a
196 question of whether GFAP interacts with fission molecules and GFAP mutations alter such
197 interaction. Under structured illumination microscopy, we found that Drp1 predominantly
198 localized in close proximity or tethered to GFAP filaments (**Fig. 5A**), suggesting that GFAP
199 filaments may act as an anchor for Drp1 oligomerization and promote the local enrichment of

200 Drp1 which drives the fission process. Quantitative analysis revealed an increased number of
201 Drp1 puncta localized to mutant GFAP compared to wildtype GFAP (**Fig. 5A-B**).
202 Immunoblotting confirmed that the increased binding in AxD astrocytes is not due to an
203 increase in the total Drp1 level (**Fig. 5C**). Furthermore, at the mitochondrial constriction sites,
204 Drp1 puncta are highly co-localized with the regions where GFAP filaments intersected
205 mitochondria (**Fig. 5D**), while a remarkable reduction of Drp1 puncta was observed on
206 mitochondria in GFAP knockout astrocytes (**fig. S3C**). Taking together, these data suggest that
207 GFAP filaments recruit or present Drp1 to mitochondria, and this hypothesis also explains the
208 phenotype of more mitochondrial fission events observed in AxD astrocytes **(Fig. 3)**.
209
210 If the GFAP-driven mitochondrial fission involves fission molecules, inhibition of Drp1
211 activity will reduce mitochondrial fission in the presence of an AxD-associated GFAP mutation.
212 Indeed, pre-incubation of AxD astrocytes with the Drp1 inhibitor Mdivi-1[29,30] rescued the
213 fragmented mitochondrial phenotype, reducing the percentage of cells with fragmented
214 mitochondria to 23%, closely resembling the isogenic control following thapsigargin washout
215 (**Fig. 5E, movie. S6**). Additionally, it resulted in tubulated mitochondria in a subset (13%) of
216 the AxD astrocytes (**Fig. 5E**).
217
218 In summary, our findings provide a previously unappreciated mechanism for mitochondrial
219 fission where intermediate filaments drive mitochondrial constriction and serve as a scaffold
220 for Drp1 (**Fig. 5F**). We provided two lines of evidence to support our model. First, GFAP
221 filaments intersect mitochondria at fission sites under physiological condition throughout the
222 entire constriction and fission process. Second, mitochondrial fission is blocked when GFAP
223 is deleted under both physiological and stimulated conditions. While actin filaments have been
224 suggested to facilitate mitochondria constriction before fission, several questions remain, such
225 as what is the mechanism for selective binding of Drp1 to actin at fission sites and whether
226 myosin provides the sole force for driving constriction[12]. Interestingly, we found that
227 mitochondria fission is inhibited even upon Ca^{2+}-induced stimulation in GFAP knockout
228 astrocytes – this observation reinforces the indispensable role of GFAP despite the fact that
229 there is acute recruitment of actin upon stimulation[11,31].
230
231 Our observation is in agreement with the potential role of intermediate filaments as a force
232 generation machinery suggested by the recent study of nuclear segmentation by vimentin[32].
233 The force generation could possibly occur through its interaction with other cytoskeletal

234 component, like actin, to drive the constriction, as implied by the interpenetration between
235 vimentin and actin filaments in the cell cortex[33,34]. Another possibility is the scaffolding
236 mechanical support that intermediate filaments provide for organelles, such as the ER. It is
237 known that ER tubules mark the sites of mitochondria division[5], and vimentin serves as a
238 scaffold for ER structure maintenance[35]. Indeed, we observed that the structure of ER was
239 drastically altered in GFAP KO (**fig. S7**). Lastly, our model raises the question of whether
240 GFAP's role in mitochondria division is a general function shared by other types of
241 intermediate filaments. It may provide a fundamental mechanism that explains/underlies
242 neurodegeneration in Alexander disease resulting from GFAP mutations.
243

244 **References**

245 1. Youle, R. J. & Bliek, A. M. Van Der. Mitochondrial Fission, Fusion, and Stress.
246 *Science.* **337**, 1062–1066 (2012).
247 2. Chan, D. C. Mitochondrial Dynamics and Its Involvement in Disease. *Annu. Rev.*
248 *Pathol. Mech. Dis.* **15**, 235–259 (2020).
249 3. Archer, S. L. Mitochondrial Dynamics — Mitochondrial Fission and Fusion in Human
250 Diseases. *N. Engl. J. Med.* **369**, 2236–2251 (2013).
251 4. Knott, A. B., Perkins, G., Schwarzenbacher, R. & Bossy-Wetzel, E. Mitochondrial
252 fragmentation in neurodegeneration. *Nat. Rev. Neurosci.* **9**, 505–518 (2008).
253 5. Friedman, J. R. *et al.* ER tubules mark sites of mitochondrial division. *Science.* **334**,
254 358–362 (2011).
255 6. Bleazard, W. *et al.* The dynamin-related GTPase Dnm1 regulates mitochondrial fission
256 in yeast. *Nat. Cell Biol.* **1**, 298–304 (1999).
257 7. Sesaki, H. & Jensen, R. E. Division versus Fusion: Dnm1p and Fzo1p Antagonistically
258 Regulate Mitochondrial Shape. *J. Cell Biol.* **147**, 699–706 (1999).
259 8. Labrousse, A. M., Zappaterra, M. D., Rube, D. A. & Van der Bliek, A. M. C. elegans
260 dynamin-related protein DRP-1 controls severing of the mitochondrial outer
261 membrane. *Mol. Cell* **4**, 815–826 (1999).
262 9. Korobova, F., Ramabhadran, V. & Higgs, H. N. An Actin-Dependent Step in
263 Mitochondrial Fission Mediated by the ER-Associated Formin INF2. *Science.* **1044**,
264 4–8 (2012).
265 10. Manor, U. *et al.* A mitochondria-anchored isoform of the actin-nucleating spire protein
266 regulates mitochondrial division. *Elife* **4:e08828**, 1–27 (2015).

267 11. Yang, C. & Svitkina, T. M. Ultrastructure and dynamics of the actin−myosin II
268 cytoskeleton during mitochondrial fission. *Nat. Cell Biol.* **21**, 603–613 (2019).
269 12. Fung, T. S., Chakrabarti, R. & Higgs, H. N. The multiple links between actin and
270 mitochondria. *Nat. Rev. Mol. Cell Biol.* **24**, 651–667 (2023).
271 13. Mose-Larsen, P., Bravo, R., Fey, S. J., Small, J. V. & Celis, J. E. Putative association
272 of mitochondria with a subpopulation of intermediate-sized filaments in cultured
273 human skin fibroblasts. *Cell* **31**, 681–692 (1982).
274 14. Herrmann, H., Bär, H., Kreplak, L., Strelkov, S. V. & Aebi, U. Intermediate filaments:
275 From cell architecture to nanomechanics. *Nat. Rev. Mol. Cell Biol.* **8**, 562–573 (2007).
276 15. Franke, W. W., Hergt, M. & Grund, C. Rearrangement of the vimentin cytoskeleton
277 during adipose conversion: Formation of an intermediate filament cage around lipid
278 globules. *Cell* **49**, 131–141 (1987).
279 16. Chang, L. *et al.* The dynamic properties of intermediate filaments during organelle
280 transport. *J. Cell Sci.* **122**, 2914–2923 (2009).
281 17. Gao, Y. S. & Sztul, E. A novel interaction of the Golgi complex with the vimentin
282 intermediate filament cytoskeleton. *J. Cell Biol.* **152**, 877–893 (2001).
283 18. Hol, E. M. & Pekny, M. Glial fibrillary acidic protein (GFAP) and the astrocyte
284 intermediate filament system in diseases of the central nervous system. *Curr. Opin.*
285 *Cell Biol.* **32**, 121–130 (2015).
286 19. Brenner, M. *et al.* Mutations in GFAP, encoding glial fibrillary acidic protein, are
287 associated with Alexander disease. *Nat. Genet.* **27**, 117–120 (2001).
288 20. Messing, A. & Brenner, M. GFAP at 50. *ASN Neuro* **12**, (2020).
289 21. Jones, J. R. *et al.* Mutations in GFAP Disrupt the Distribution and Function of
290 Organelles in Human Astrocytes. *Cell Rep.* **25**, 947-958.e4 (2018).
291 22. Krencik, R., Weick, J. P., Liu, Y., Zhang, Z. J. & Zhang, S. C. Specification of
292 transplantable astroglial subtypes from human pluripotent stem cells. *Nat. Biotechnol.*
293 **29**, 528–534 (2011).
294 23. Mitra, K., Wunder, C., Roysam, B., Lin, G. & Lippincott-Schwartz, J. A hyperfused
295 mitochondrial state achieved at G1-S regulates cyclin E buildup and entry into S
296 phase. *Proc. Natl. Acad. Sci. U. S. A.* **106**, 11960–11965 (2009).
297 24. Rambold, A. S., Kostelecky, B., Elia, N. & Lippincott-Schwartz, J. Tubular network
298 formation protects mitochondria from autophagosomal degradation during nutrient
299 starvation. *Proc. Natl. Acad. Sci. U. S. A.* **108**, 10190–10195 (2011).
300 25. Smirnova, E., Griparic, L., Shurland, D.-L. & Van Der Bliek, A. M. Drp1 Is Required

301 for Mitochondrial Division in Mammalian Cells. *Mol. Biol. Cell* **12**, 2245–2256
302 (2001).
303 26. Chen, H. *et al.* Mitofusins Mfn1 and Mfn2 coordinately regulate mitochondrial fusion
304 and are essential for embryonic development. *J. Cell Biol.* **160**, 189–200 (2003).
305 27. Hom, J. R., Gewandter, J. S., Michael, L., Sheu, S.-S. & Yoon, Y. Thapsigargin
306 induces biphasic fragmentation of mitochondria through calcium-mediated
307 mitochondrial fission and apoptosis. *J. Cell. Physiol.* **212**, 498–508 (2007).
308 28. Cereghetti, G. M. *et al.* Dephosphorylation by calcineurin regulates translocation of
309 Drp1 to mitochondria. *Proc. Natl. Acad. Sci. U. S. A.* **105**, 15803–15808 (2008).
310 29. Cassidy-Stone, A. *et al.* Chemical Inhibition of the Mitochondrial Division Dynamin
311 Reveals Its Role in Bax/Bak-Dependent Mitochondrial Outer Membrane
312 Permeabilization. *Dev. Cell* **14**, 193–204 (2008).
313 30. Bordt, E. A. *et al.* The Putative Drp1 Inhibitor mdivi-1 Is a Reversible Mitochondrial
314 Complex I Inhibitor that Modulates Reactive Oxygen Species. *Dev. Cell* **40**, 583-
315 594.e6 (2017).
316 31. Chakrabarti, R. *et al.* INF2-mediated actin polymerization at the ER stimulates
317 mitochondrial calcium uptake, inner membrane constriction, and division. *J. Cell Biol.*
318 **217**, 251–268 (2018).
319 32. Liu, J. *et al.* Vimentin regulates nuclear segmentation in neutrophils. *Proc. Natl. Acad.*
320 *Sci.* **120**, (2023).
321 33. Wu, H. *et al.* Vimentin intermediate filaments and filamentous actin form unexpected
322 interpenetrating networks that redefine the cell cortex. *Proc. Natl. Acad. Sci. U. S. A.*
323 **119**, 1–10 (2022).
324 34. Jiu, Y. *et al.* Bidirectional Interplay between Vimentin Intermediate Filaments and
325 Contractile Actin Stress Fibers. *Cell Rep.* **11**, 1511–1518 (2015).
326 35. Cremer, T. *et al.* RNF26 binds perinuclear vimentin filaments to integrate ER and
327 endolysosomal responses to proteotoxic stress . *EMBO J.* **42**, 1–24 (2023).
328 36. Chambers, S. M. *et al.* Highly efficient neural conversion of human ES and iPS cells
329 by dual inhibition of SMAD signaling. *Nat. Biotechnol.* **27**, 275–280 (2009).
330 37. Roth, S. & Heintzmann, R. Optical photon reassignment with increased axial
331 resolution by structured illumination. *Methods Appl. Fluoresc.* **4**, 045005 (2016).
332
333

Acknowledgments

We would like to thank Emma Feng for assistance with imaging.

Funding:

Singapore Ministry of Education, MOE2018-T2-2-103 (S-C.Z.)
Duke-NUS medical school, Duke-NUS-KPFA/2018/0022 (D.X.)
Singapore Ministry of Health, MOH-000207 and 000212 (S-C.Z.)
National Institute of Health, HD076892 (A.M.)
National Institute of Health, HD090256 (A.M.)
National Institute of Health, HD106197 (S-C.Z.)
Aligning Science Across Parkinson's, ASAP-000301 (S-C.Z.)
Natural Science Foundation of China, 82301042 (D.X.)
Sichuan Science and Technology Program 2023ZYD0065 and 2023NSFSC0565 (D.X.)

Author contributions:

Conceptualization: SCZ, DX, LHK
Methodology: DX, LHK, YST
Investigation: DX, YST, LHK, XL, EA
Visualization: DX, YST, LHK, FY
Funding acquisition: SCZ, AM, DX
Supervision: SCZ
Writing-original draft: DX, SCZ, LHK, YST, FY
Writing-review and editing: DX, SCZ, LHK, ZJS, FY, AM

Competing interests: Authors declare no competing interests. S-C.Z. is a co-founder of BrainXell, Inc.

Supplementary Materials

Materials and Methods

Figs. S1 to S7

Movies S1 to S6

Figure 1

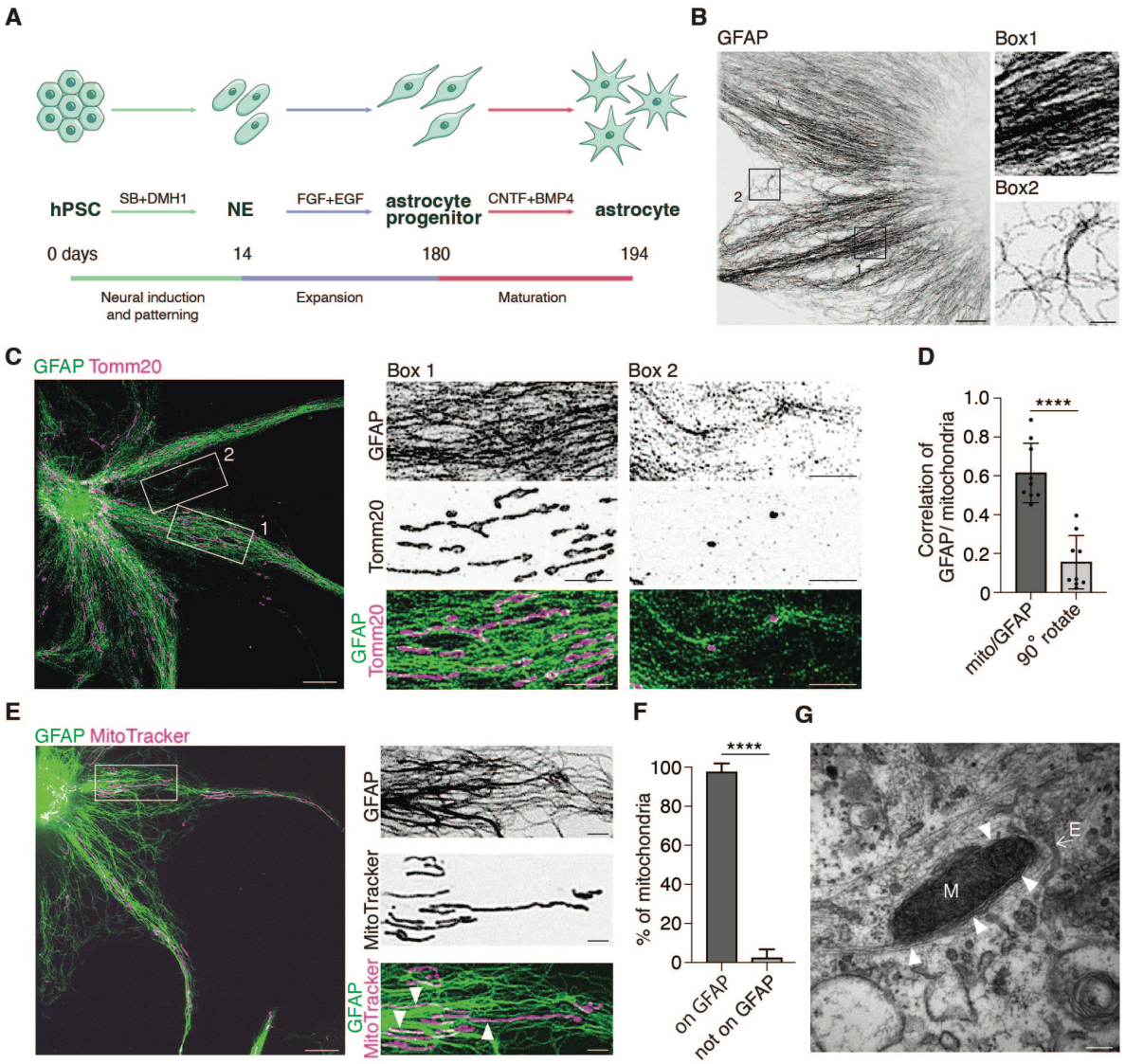

Fig. 1. Spatial relationship between mitochondria and GFAP filaments. (**A**) Schematic of astrocyte generation from human PSCs (hPSCs). (**B**) Representative single-z SIM image of an astrocyte generated from H1 cell line immunostained with an antibody against GFAP. Boxes 1-2 mark regions of GFAP filaments at a higher magnification showing GFAP bundles (Box 1) and individual filaments (Box 2). (**C**) SIM image shows astrocyte co-immunostained with antibodies against GFAP (green) and Tomm20 (magenta). Area of GFAP bundles (Box 1) and individual filaments (Box 2) with Tomm20 are shown at higher magnification. (**D**) The level of colocalization between endogenous GFAP and mitochondria was determined by measuring the Mander's coefficient for Tomm20 over GFAP, or when Tomm20 image was rotated 90° (****, $p \leq 0.0001$, two-tailed paired *t*-test, n=9 cells). (**E**) Representative SIM image showing H1 astrocyte expressing GFAP-mNeon and stained with MitoTracker. An area of GFAP and mitochondria (white box) is shown in high-magnification images. Arrowheads indicate the positions of mitochondria aligned with GFAP filaments. (**F**) Quantification of the percentage of mitochondria aligned with GFAP filaments (196 mitochondria from 5 cells; $p \leq 0.0001$, two-tailed paired *t*-test). (**G**) Representative transmission electron microscopy (TEM) image

showing mitochondria (M), GFAP filaments (arrowhead) and ER (E, white arrow). Scale bar: SIM images, 10 μm; zoom-in SIM images, 2 μm; TEM image, 200 nm.

Figure 2

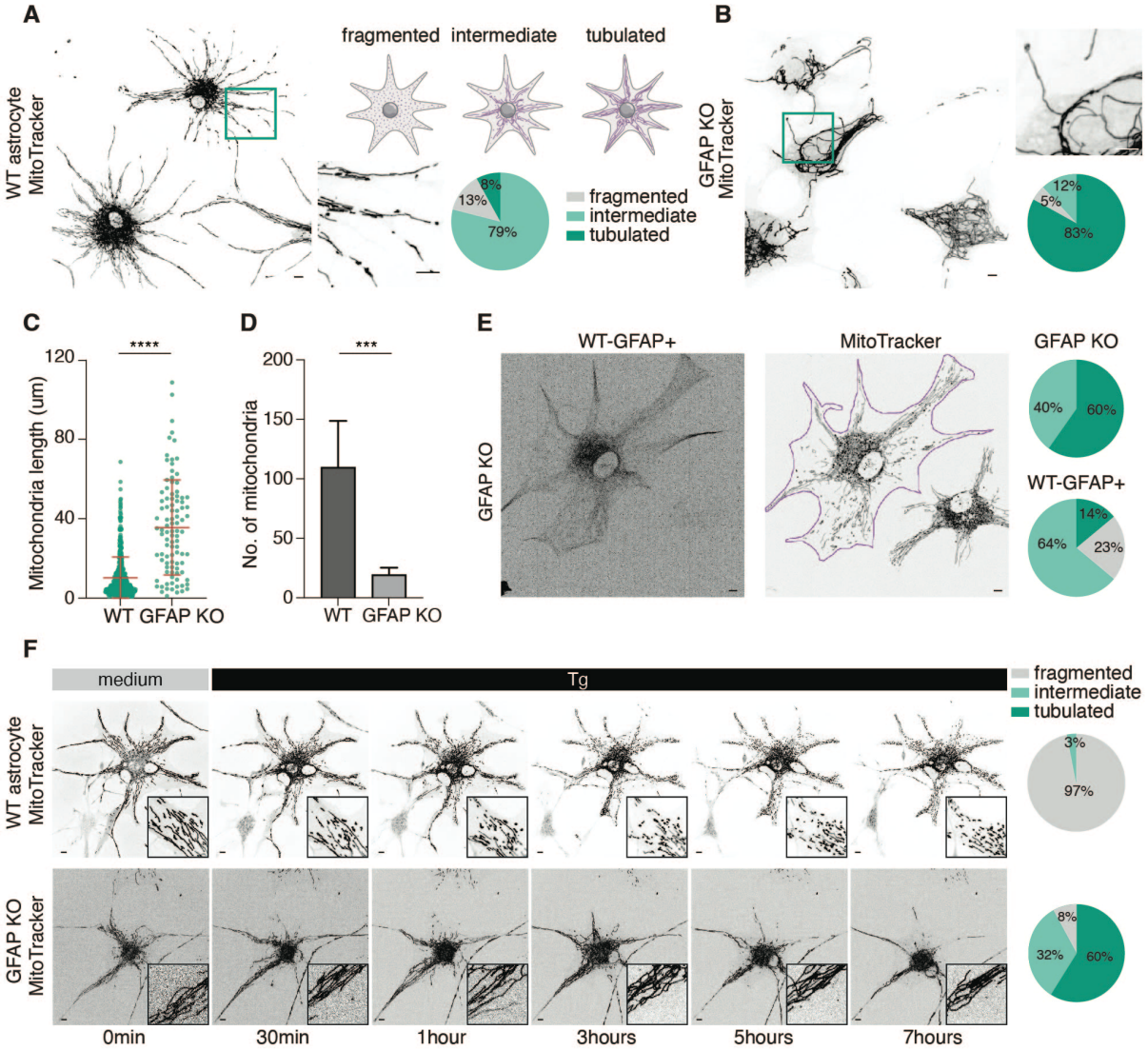

Figure 2. Inhibition of mitochondrial fission in GFAP knockout astrocytes. (**A**) Representative confocal image, magnified image of inset, and percentage of cells with indicated mitochondrial morphologies from wildtype astrocytes stained with MitoTracker (n=122 cells, 3 independent experiments). Mitochondria were visually scored as fragmented, intermediate or tubulated, as in the diagram. (**B**) Representative confocal image, magnified image of inset, and percentage of cells with indicated mitochondrial morphologies from GFAP knockout astrocytes stained with MitoTracker (n=144 cells, 5 independent experiments). (**C-D**) Quantification of individual mitochondrial length (**C**) and the number of mitochondria (**D**) in single astrocytes from WT and GFAP knockout astrocytes (549 and 97 mitochondria from 5 cells for WT and GFAP knockout cells, respectively). (**E**) Representative confocal images and percentage of cells with indicated mitochondrial morphologies in GFAP knockout astrocytes expressing WT-GFAP. Images showed GFAP KO astrocytes transfected with WT-GFAP-mNeon and stained with MitoTracker. Astrocyte with GFAP expression is outlined in purple. Percentage of cells with indicated mitochondrial morphologies from GFAP knockout and WT-GFAP expressing astrocytes from the same dish (149 GFAP KO cells and 83 GFAP expressing cells, 3 independent experiments). (**F**) Live-cell images and magnified images of

WT and GFAP knockout astrocytes stained with MitoTracker when treated with 2 μM thapsigargin. Percentage of cells with indicated mitochondrial morphologies is shown at the right panel (62 WT and 119 GFAP KO cells, 3 independent experiments). ****, p ≤0.0001; ***, p≤0.001 by two-tailed unpaired *t*-test. Scale bar, 10 μm.

Figure 3

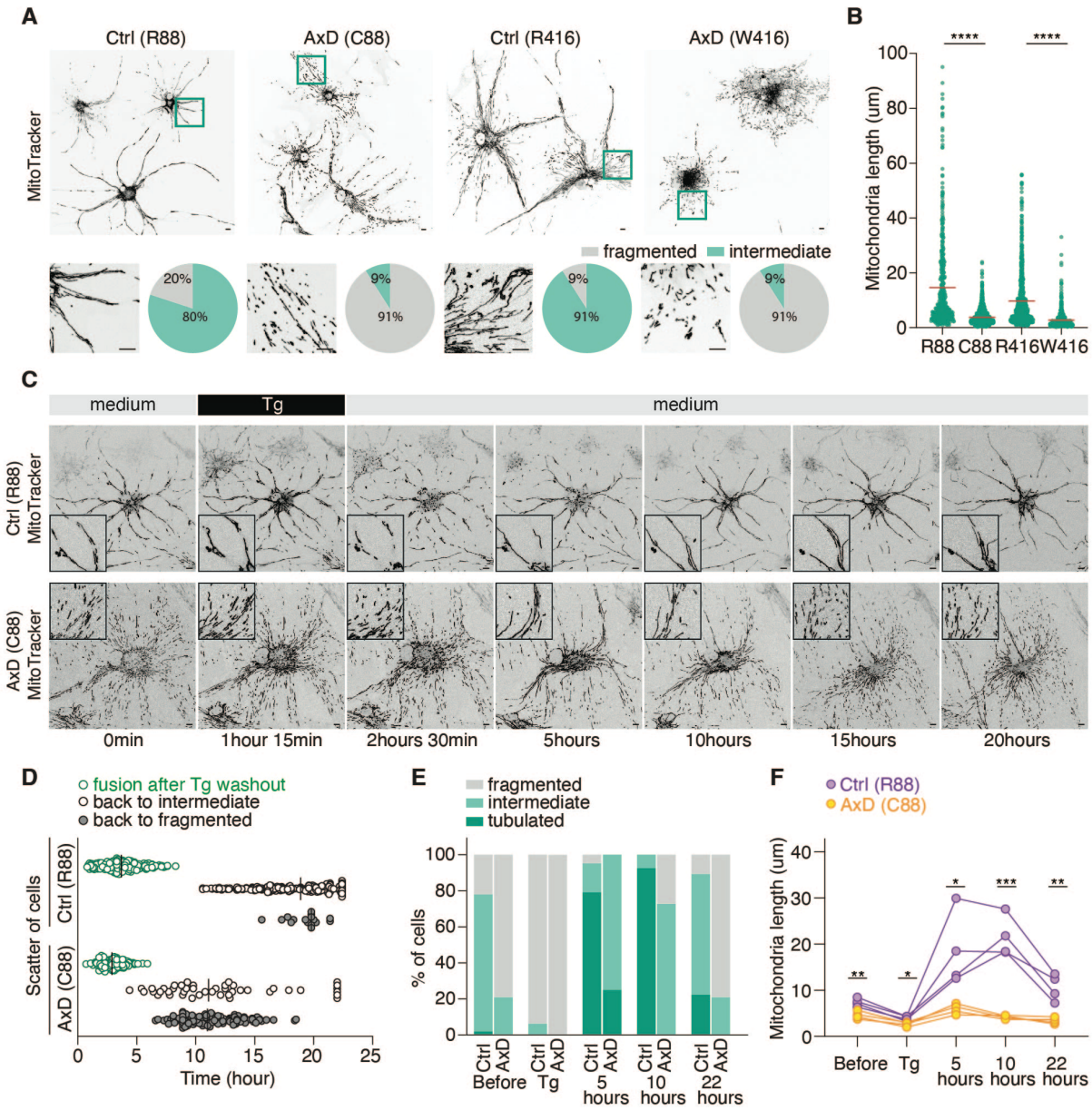

Figure 3. Mitochondrial fission is enhanced by AxD mutations. (**A**) Representative confocal images and percentage of cells with indicated mitochondrial morphologies in C88 and W416 AxD astrocytes and their isogenic controls R88 and R416. Astrocytes are stained with MitoTracker and insets are magnified below (n=188 R88 cells and 194 C88 cells from 11 independent experiments; n=140 R416 cells and 119 W416 cells, 4 independent experiments). (**B**) Quantification of individual mitochondrial length for both pairs of isogenic AxD astrocytes (n=524, 1705, 770 and 650 mitochondria from 5 cells for R88, C88, R416 and W416, respectively). (**C**) Live-cell images showing the dynamics of mitochondrial fission-fusion in control (R88) and AxD (C88) astrocytes. Astrocytes stained with MitoTraker are synchronized by 2 μM thapsigargin and exchanged back to normal medium as indicated. (n=186 R88 cells

416 and 151 C88 cells, 3 independent experiments). (**D**) Scatter plot shows the time point at which
417 mitochondria start fusion after thapsigargin washout (green), return back to intermediate
418 mitochondria status (black circle) or further go back to fragmented status (grey). Each dot
419 represents one cell, with average time shown as black lines. (**E**) Percentage of R88 and C88
420 astrocytes in tubulated (green), intermediate (light green) and fragmented (grey) status at
421 indicated time. 92% (172/186) control astrocytes and 25% (37/151) AxD astrocytes form
422 hyperfused mitochondria before return back to intermediate or fragmented status. (**F**)
423 Quantification of individual mitochondrial length for R88 and C88 astrocytes at indicated time.
424 One dot means averaged mitochondria length from one cell (4 cells for R88 and C88 cells,
425 respectively). The plot for the length of individual mitochondria is shown in fig. S5B. *,
426 $p<0.05$, **, $p<0.005$, ***, $p<0.001$ by two-tailed unpaired *t*-test. Scale bar, 10 μm.

Figure 4

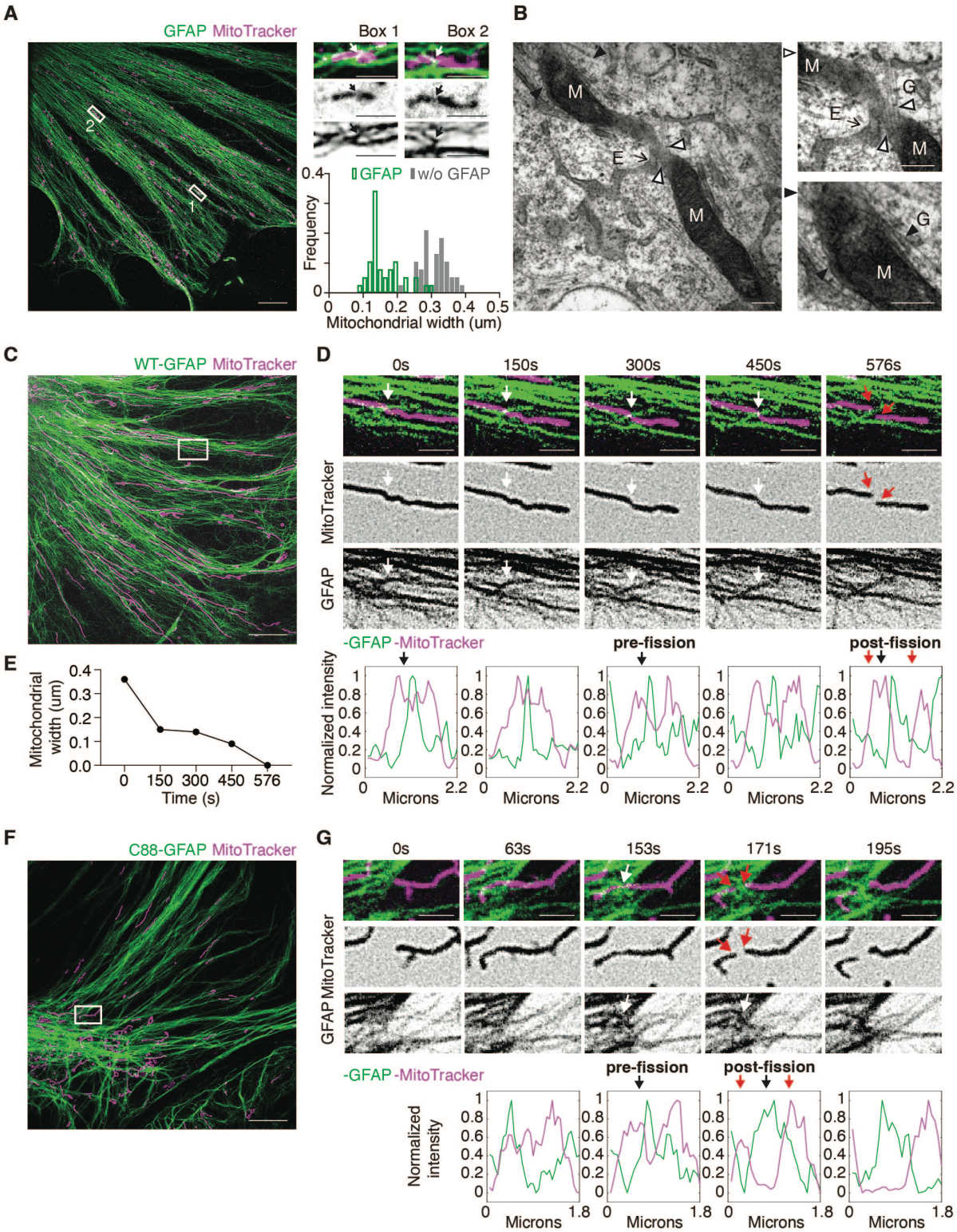

Figure 4. GFAP filaments directly participate in mitochondrial constriction. (**A**) Representative SIM image and histogram for mitochondrial diameter of R88 control astrocytes immunostained for GFAP (Cell signaling technology, 34001) and stained with MitoTracker. Insets are magnified on the top right. Arrows indicate the regions where GFAP filaments cross mitochondria. Histogram at the bottom right showing diameter of mitochondria with or without GFAP crossing (with GFAP: n=38 events, without GFAP: n=38 events, 8 independent experiments) (**B**) Representative transmission electron microscopy (TEM) image with zoom-

435 in panels showing GFAP filaments aligned in parallel (black arrowhead) with mitochondria
436 (M) or crossing (white arrowhead) mitochondria next to ER (E). (**C**) SIM image of a live
437 astrocyte expressing WT-GFAP-mNeon and stained with MitoTracker. (**D**) Upper, high-
438 magnification images of the selected region in (C) showing GFAP filament crossing the site of
439 mitochondrial division (white arrow) before fission (red arrow). Dashed line indicates the
440 mitochondrial region used to generate line scan plot. Bottom, corresponding line scans analyze
441 the fluorescence intensity of mitochondria and GFAP pre- and post-fission. Black and red
442 arrows on line scan analysis correspond to white arrow and red arrow positions at pre-
443 constriction and division sites, respectively (44/53 mitochondria with WT-GFAP crossing, 4
444 independent experiments). (**E**) Quantification of corresponding mitochondrial width at the
445 position of GFAP crossing (white arrows) in (D). (**F-G**) As in (C-D), SIM images, high-
446 magnification and line scan analysis of a live astrocyte expressing C88-GFAP- mNeon and
447 stained with MitoTracker (24/28 mitochondria with C88-GFAP crossing, 3 independent
448 experiments). Scale bar: SIM images, 10 μm; zoom-in SIM images, 2 μm; TEM image, 200
449 nm.

Figure 5

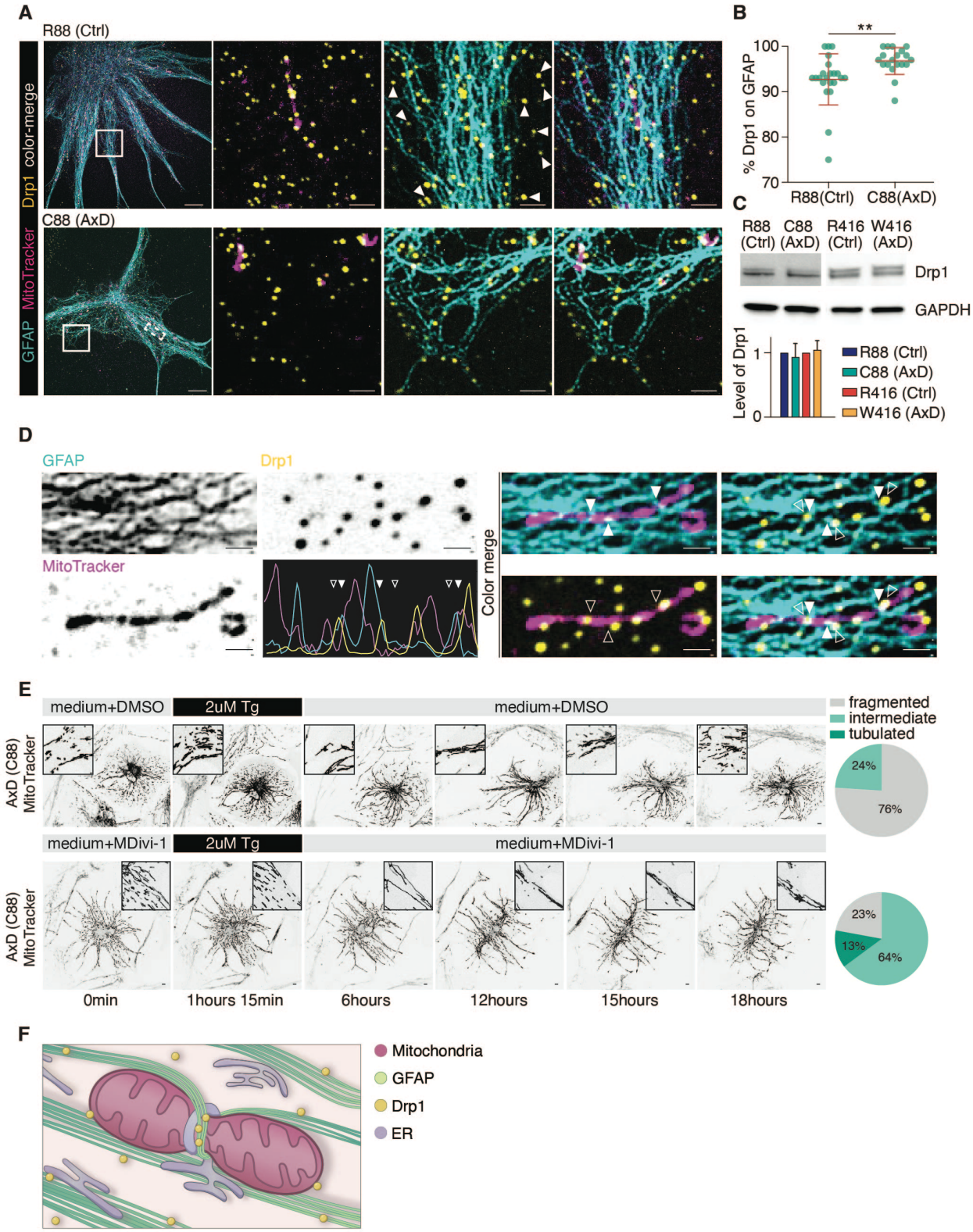

Figure 5. GFAP filaments serve as scaffolds for fission protein Drp1. (**A**) SIM images and high-magnification view of C88 AxD and isogenic control astrocytes immunostained for GFAP (Cell signaling technology, 34001) and Drp1, and stained with MitoTracker. White arrows indicate the Drp1 punctae that do not correlate with GFAP filaments. (**B**) Percentage of Drp1 puncta located on GFAP filaments (22 and 19 regions for control and AxD astrocytes, respectively). (**C**) Western blot and quantification showing the protein level of Drp1 in isogenic

457 controls and AxD astrocytes (n=3 independent experiments). (**D**) High-magnification view and
458 line scan analysis along mitochondria showing GFAP filaments and Drp1 puncta in
459 mitochondrial constriction, originated from dashed line box in (C). Arrowheads in images and
460 linescan highlight GFAP and Drp1 (white) positioned at mitochondria constriction sites
461 (hollow). (**E**) Live-cell images and percentage of cells with indicated mitochondrial
462 morphologies showing C88 AxD astrocytes mitochondrial change upon 2 μM thapsigargin.
463 Cells are pre-incubated in medium with MDivi-1/DMSO, treated with thapsigargin and
464 returned to medium with Mdivi-1/DMSO at indicated times (n=82 and 41 AxD cells for Mdivi-
465 1 and DMSO incubation, respectively, 3 independent experiments). (**F**) Schematic
466 representation showing the role of GFAP during mitochondria fission. **, $p<0.005$ by two-
467 tailed unpaired *t*-test. Scale bar: confocal and SIM images, 10 μm, zoom-in SIM images, 2 μm.